

Filamentation of femtosecond light pulses in the air: Turbulent cells versus long-range clustersS. Skupin,^{1,2,*} L. Bergé,¹ U. Peschel,² F. Lederer,² G. Méjean,³ J. Yu,³ J. Kasparian,³ E. Salmon,³ J. P. Wolf,³ M. Rodriguez,⁴ L. Wöste,⁴ R. Bourayou,⁵ and R. Sauerbrey⁵¹*Département de Physique Théorique et Appliquée, CEA/DAM Ile de France, Boîte Postale 12, 91680 Bruyères-le-Chatel, France*²*Institut für Festkörperteorie und Theoretische Optik, Friedrich-Schiller-Universität Jena, Max-Wien-Platz 1, 07743 Jena, Germany*³*Laboratoire de Spectrométrie Ionique et Moléculaire, Université Cl. Bernard Lyon 1, UMR-CNRS 5579, F-69622 Villeurbanne Cedex, Lyon, France*⁴*Institut für Experimentalphysik, Freie Universität Berlin, Arnimallee 14, D-14195 Berlin, Germany*⁵*Institut für Optik und Quantenelektronik, Friedrich-Schiller-Universität Jena, Max-Wien-Platz 1, 07743 Jena, Germany*

(Received 30 January 2004; revised manuscript received 13 May 2004; published 5 October 2004)

The filamentation of ultrashort pulses in air is investigated theoretically and experimentally. From the theoretical point of view, beam propagation is shown to be driven by the interplay between random nucleation of small-scale cells and relaxation to long waveguides. After a transient stage along which they vary in location and in amplitude, filaments triggered by an isotropic noise are confined into distinct clusters, called “optical pillars,” whose evolution can be approximated by an averaged-in-time two-dimensional (2D) model derived from the standard propagation equations for ultrashort pulses. Results from this model are compared with space- and time-resolved numerical simulations. From the experimental point of view, similar clusters of filaments emerge from the defects of initial beam profiles delivered by the Teramobile laser facility. Qualitative features in the evolution of the filament patterns are reproduced by the 2D reduced model.

DOI: 10.1103/PhysRevE.70.046602

PACS number(s): 52.38.Hb, 42.65.Tg, 42.65.Jx, 42.68.Ay

I. INTRODUCTION

First experiments on the long-range propagation of femtosecond (fs) laser pulses were performed in the mid-1990s [1–3]. In these experiments, infrared laser pulses with duration of about 100 fs produced narrow filaments of several meters, along which more than 10% of the energy was observed to be localized in the near-axis area. This phenomenon is attributed to the early self-focusing of laser radiation, which originates from the Kerr response of air and leads to an increase of light intensity. This growth is then saturated by the defocusing action of the electron plasma created by photoionization of air molecules. As a result, the maximum light intensity in the filament does not exceed 10^{14} W/cm² for infrared pulses. If the pulse power is less than a few critical powers for self-focusing (P_{cr}) in air [1,2], only one filament is created. At higher powers, two or more filaments can be produced [3–7]. Knowing that novel optical sources nowadays access the terawatt (TW) range, it is thus timely to understand the dynamics of fs light pulses when they decay into multiple small-scale structures, in view of improving, e.g., atmospheric remote sensing techniques [8].

Filaments originate from the modulational instability (MI) triggered by the nonlinear response of air. Applied to an optical background, MI breaks up high-power beams into small-scale cells that each convey a power close to $P_{fil} \approx \pi^2 P_{cr}/4$ [9–11]. These cells are then amplified through the collapse dynamics and relax their inner power to the critical one, until they reach the ionization threshold near which they give rise to various transverse patterns and undergo strong temporal distortions [11,12]. At relatively low energies

(≤ 5 mJ), a beam can decompose only into a couple of small spots that fuse as they attain a full ionization regime [5]. This fusion mechanism reduces the final number of output filaments along the propagation axis. For broader beams conveying much higher energies, another scenario [13], elaborated from three-dimensional (3D) numerical simulations of a central portion of the pulse over a dozen of meters, emphasizes a propagation sustained by random nucleation of small-scale filaments: Collapsing cells resulting from MI are regularized via plasma defocusing with very weak losses from multiphoton absorption (MPA). Recurrent collapse events, which are fed by the energy reservoir created from anterior defocused filaments, then form an “optically turbulent light guide,” which drives the pulse dynamics. This latter scenario contrasts with the simple picture of light guides that stay robust over long distances.

The goal of this work is to clear up this apparent controversy by investigating pulse filamentation up to the Rayleigh range for high input powers ($10 < P_{in}/P_{cr} < 1000$). To address this issue, we first briefly recall the fundamental equations governing the atmospheric propagation of ultrashort pulses. Because the numerical integration of these equations over long distances in full (3D+1)-dimensional geometry is mostly limited by the available computer capacities, we propose a (2D+1)-dimensional model derived by averaging all time dependencies in the laser envelope and the plasma response. This reduced model [7] admits solitonlike states that describe short-range “randomly-nucleated” filaments. We show that these structures confine themselves into a limited number of long-range coherent objects, termed as “optical pillars.” Besides transient stages where turbulent cells recur, these new structures around which filaments self-organize drive the pulse dynamics. This property is confirmed by the direct solving of the (3D+1)-dimensional equations applied

*Electronic address: stefan@pinet.uni-jena.de

to mm-waisted ultrashort pulses. Second, we compare experiments with numerical simulations in order to understand how filaments are produced and how they impact on the long-distance propagation of TW pulses with peak powers as high as 1000 times P_{cr} . To do so, three series of experiments involving the Teramobile facility [14] are performed in parallel geometry, with beam powers varying between 120 and 1000 P_{cr} . Each series of experiments is numerically simulated by means of the averaged-in-time approach. This model is found to reproduce the qualitative features of the experimental patterns. High-intensity defects in the spatial distribution of the input beam generate “optical pillars” persisting over several tens of meters through the propagation. By “optical pillars” we mean discrete light spots capable of amalgamating short-living solitonlike cells that self-attract around specific points in the diffraction plane. The resulting structure then sustains a long-range propagation, while it can still continue to excite short-range cells in its vicinity. Optical pillars indeed evacuate power as they collapse, so that randomly nucleated filaments may recur more and more along the optical path, in accordance with the scenario of [13]. The major difference between the concept of “optical pillars” and both the “optically-turbulent light guide” [13] and “self-waveguiding” [1] models lies in the following: The possibility of guiding the beam through a small number of quasicontinuous long-range clusters created from its most intense regions. A last experiment realized in converging geometry validates this concept: A focused beam is observed to decay into several tens of small-scale cells before the focal point of the beam. The linear lensing shrinks all filaments at the focal point, after which only three quasicontinuous channels of light keeping the same average direction propagates over almost 10 m.

The paper is organized as follows. In Sec. II we briefly recall the model equations. Section III is devoted to the derivation of the reduced (2D+1)-dimensional model and to the analysis of its solitonlike solutions. Emphasis is put on soliton interactions in the conservative regime and on the action of MPA which damps the soliton profiles and decreases their power over a generic distance. In spite of natural limitations owing to the averaging in time, the spatial dynamics described by this model is found to be qualitatively close to that provided by the original (3D+1)-dimensional equations. Direct comparisons between both models are commented on in Sec. IV, where the limits of applicability for the 2D reduction are thoroughly discussed. Differences between an averaged-in-time filament compared with its (3D+1) counterpart developing a two-peaked temporal profile [15,16] are discussed. Section V concerns experimental observations of filaments evolving from terawatt pulses delivered by the Teramobile facility. By means of classical charge coupled device (CCD) imaging, the filamentation figures are collected over regular distances upon the propagation axis. They emphasize the early amplification of the initial beam defects. These defects then serve as central “hot” spots around which short-scale light cells arise and rapidly recur over 1 m-range distances. The local zones formed by a central spot surrounded by short-living cells are able to propagate much farther and meet the definition of an “optical pillar” given above. The qualitative events developed in the experimental

patterns are shown to agree with numerical computations realized from the 2D reduced model, using a digitized file of the input beam profile. Different input powers comprised between 100 and 1000 times P_{cr} are investigated for collimated beams. A special experiment involving a focused beam achieves to confirm both the validity of the 2D model and the existence of “optical pillars.”

II. THE PHYSICAL MODEL

The equations describing the propagation of ultrashort pulses with intensities limited to 10^{14} W/cm² at infrared wavelengths are nowadays classical. As already justified in anterior references [5,7,12,13,15–17], the fundamental model consists of a (3D+1)-dimensional extended nonlinear Schrödinger (NLS) equation for the electric field envelope $\mathcal{E}(x, y, z, t)$ moving with the group velocity v_g , coupled to a Drude model for the local plasma density $\rho(x, y, z, t)$:

$$\frac{\partial \mathcal{E}}{\partial z} = \frac{i}{2k_0} \nabla_{\perp}^2 \mathcal{E} - i \frac{k''}{2} \partial_t^2 \mathcal{E} + ik_0 n_2 \mathcal{R}(t) \mathcal{E} - \left(\frac{\sigma}{2} + i \frac{k_0}{2\rho_c} \right) \rho \mathcal{E} - \frac{\beta^{(K)}}{2} |\mathcal{E}|^{2K-2} \mathcal{E}, \quad (1a)$$

$$\mathcal{R}(t) = (1 - \theta) |\mathcal{E}|^2 + \frac{\theta}{\tau_K} \int_{-\infty}^t e^{-(t-t')/\tau_K} |\mathcal{E}(t')|^2 dt', \quad (1b)$$

$$\partial_t \rho = \sigma_K \rho_{\text{nl}} |\mathcal{E}|^{2K} + \frac{\sigma}{U_i} \rho |\mathcal{E}|^2. \quad (1c)$$

These equations apply to fs pulses moving in their group-velocity frame ($t \rightarrow t - z/v_g$), with the central wave number $k_0 = 2\pi/\lambda_0$. The critical power for self-focusing is defined by $P_{\text{cr}} = \lambda_0^2 / 2\pi n_2$ and in air it takes the value $P_{\text{cr}} \approx 3.3$ GW for the laser wavelength $\lambda_0 = 800$ nm and Kerr refraction index $n_2 = 3.2 \times 10^{-19}$ cm²/W. In Eq. (1a), z is the longitudinal distance of propagation while $\nabla_{\perp}^2 = \partial_x^2 + \partial_y^2$ accounts for optical diffraction in the (x, y) plane. The second-order temporal derivative refers to normal group-velocity dispersion (GVD) with the coefficient $k'' = 0.2$ fs²/cm. The complete Kerr response of air, defined by Eq. (1b), is composed of an instantaneous contribution and a delayed part in ratio θ , with a relaxation time $\tau_K = 70$ fs [5,17]. The quantity $\rho_c = 1.8 \times 10^{21}$ cm⁻³ is the critical plasma density beyond which the beam no longer propagates. Power dissipation is assured by multiphoton absorption (MPA) with coefficient $\beta^{(K=8)} = 4.25 \times 10^{-98}$ cm¹³/W⁷ [15,17]. In Eq. (1c), plasma defocusing is mainly induced by ionization of oxygen molecules with gap potential $U_i = 12.1$ eV, contributing to 20% of the neutral density $\rho_{\text{at}} = 2.7 \times 10^{19}$ cm⁻³ [17], so that the effective density of neutral molecules is given by $\rho_{\text{nt}} = 5.4 \times 10^{18}$ cm⁻³. The number of photons K needed to extract electrons from neutral atoms is then $K = 8$. The electron plasma is essentially driven by multiphoton ionization (MPI) with coefficient $\sigma_{K=8} = 2.88 \times 10^{-99}$ s⁻¹ cm¹⁶/W⁸. Avalanche (cascade) ionization and plasma absorption identified by the cross section for inverse bremsstrahlung $\sigma = 5.44 \times 10^{-20}$ cm² complete this model.

III. THE REDUCED 2D MODEL

In the following, we consider input electric field distributions characterized by a beam waist w_0 , half-width duration t_p , and Rayleigh length $z_0 = \pi w_0^2 / \lambda_0$.

A. Derivation

Current limitations of even the most modern, massively parallel computer machines still prevent us from accessing a complete description of a km-range propagation of broad, cm-waisted beams as a whole, in reasonable CPU times. For, e.g., a beam waist of about 2.5 cm only and a pulse duration ~ 100 fs, the appropriate resolution would require at least 2^{37} mesh points for numerical box lengths in (x, y, t) of 15×15 cm² and 600 fs, respectively. In addition, it is often necessary to employ an adaptively refined step along z able to resolve correctly the sharp peaks coupled to narrow plasma channels with size ≤ 50 μm , emerging along the filamentation process. Numerical simulations fulfilling these needs then consume several Terabytes in memory for a single run, which we have to avoid. For this reason, we may alternatively derive a reduced model from the original (3D+1)-dimensional equations. This model amounts to reducing the number of effective dimensions by freezing suitably the temporal dependencies of the wave field. Even though this reduction is primarily motivated by technical constraints, it also allows us to gain a deeper insight into the transverse dynamics of the filamentation phenomenon.

To establish the 2D model, we first apply some preliminary approximations. Considering subpicosecond durations, avalanche ionization and related plasma absorption have a weak incidence on the pulse dynamics for the parameters examined below and we thus ignore them. We can also omit group-velocity dispersion, whose physical coefficient $k'' = 0.2$ fs²/cm makes it too weak for being a key player competing with ionization of air molecules over filamentation distances limited to 100 m. Former numerical simulations in this field showed that femtosecond filaments result from the competition between Kerr self-focusing and MPI. We thus assume that MPI mainly counterbalances Kerr self-focusing at a time slice $t \approx t_c(z)$ where a dominant spike with temporal extent T emerges in the pulse temporal profile. This duration T is conjectured to keep the same order of magnitude along propagation. Therefore we decompose \mathcal{E} as follows:

$$\mathcal{E}(x, y, z, t) = \psi(x, y, z) \times \chi[t, t_c(z)], \quad (2)$$

where the temporal distribution for the highest-intensity peak is modeled by the Gaussian $\chi[t, t_c(z)] = e^{-[t - t_c(z)]^2 / T^2}$. Under the previous hypotheses, we can plug the above expression of \mathcal{E} into Eq. (1), use the expression of

$$\rho \approx \sqrt{\frac{\pi}{8K}} T \sigma_K \rho_{\text{nl}} |\psi|^{2K} \left\{ \text{erf} \left[\frac{\sqrt{2K} [t - t_c(z)]}{T} \right] + 1 \right\}$$

where $\text{erf}(x)$ denotes the usual error function, and integrate Eq. (1a) over the entire time domain after multiplying it by χ . The resulting equation for ψ reads

$$\frac{\partial \psi}{\partial z} = \frac{i}{2k_0} \nabla_{\perp}^2 \psi + i \alpha k_0 n_2 |\psi|^2 \psi - i \gamma |\psi|^{2K} \psi - \frac{\beta^{(K)}}{2\sqrt{K}} |\psi|^{2K-2} \psi, \quad (3)$$

where $\alpha = (1 - \theta + \theta D / \sqrt{2} \tau_K) / \sqrt{2}$, $\gamma = \sqrt{\pi / 8K} (T k_0 \sigma_K \rho_{\text{nl}}) / (2\rho_c)$, and

$$D = \int_{-\infty}^{+\infty} e^{T^2/8\tau_K^2 - u/\tau_K - 2u^2/T^2} \left[\text{erf} \left(\frac{\sqrt{2}u}{T} - \frac{T}{\sqrt{8}\tau_K} \right) + 1 \right] du.$$

Here, the integral D follows from averaging in time the delayed Kerr component, where, in agreement with antecedent studies (see, e.g., Refs. [5,17]), we shall henceforth impose $\theta = 1/2$. Equation (3) describes the transverse dynamics of fs beams, with appropriate coefficients α , γ keeping the trace of averaged variations in time of the pulse. It is worth noticing that this model does not depend on the longitudinal location of the time slice $t = t_c(z)$. The only arbitrariness is the choice of the peak duration T . On the one hand, a natural assumption would be to opt for $T = t_p$, i.e., an ionization front raises from a wave structure with mean duration comparable to that of the input pulse. For example, when $t_p = 85$ fs and $\tau_K = 70$ fs, this choice leads to $D \approx 0.707$ and $\alpha \approx 0.57$. On the other hand, there now exists evidence [15,18] that MPI can shorten pulses to mean duration reaching 1/10 of their initial values. Setting $T = 0.1 t_p$ with $t_p = 85$ fs then provides the coefficients $D = 0.117$, so that $\alpha = 0.39$. Note from these estimates that the global effect of the delayed Kerr component is to increase the effective power for self-focusing to some extent. This property may explain former experimental observations [1], following which powers above three times P_{cr} are often necessary to create one localized filament. Because we wish to describe filamentation patterns in a full ionization regime, we henceforth assume $T = t_p / 10$. This value was found to provide the best approximations of fluence patterns developed by (3D+1)-dimensional fs pulses.

Let us now discuss inherent properties to Eq. (3) before proceeding to comparisons of this 2D approach with direct simulations of Eq. (1).

B. Solitonlike dynamics

For technical convenience, we express Eq. (3) into a dimensionless system of units. Only employed in this section, this change of variables and fields fixes the saturation intensity (I_{max}) realizing an equilibrium between Kerr and MPI nonlinearities to the unity. By introducing the rescaled variables $Z = z [(\alpha k_0 n_2)^K / \gamma]^{1/(K-1)}$, $X = x \sqrt{2k_0} [(\alpha k_0 n_2)^K / \gamma]^{1/(2K-2)}$, $Y = y \sqrt{2k_0} [(\alpha k_0 n_2)^K / \gamma]^{1/(2K-2)}$, the rescaled field $A = \psi (\gamma / \alpha k_0 n_2)^{1/(2K-2)}$, and the parameter $\nu = (\beta^{(K)} / 2\sqrt{K}) \times (\alpha k_0 n_2 \gamma^{K-2})^{1/(1-K)}$, it is straightforward to rewrite Eq. (3) in the form

$$\frac{\partial A}{\partial Z} = i \Delta_{\perp} A + i |A|^2 A - i |A|^{2K} A - \nu |A|^{2K-2} A, \quad (4)$$

where $\Delta_{\perp} = \partial^2 / \partial X^2 + \partial^2 / \partial Y^2$ and the parameter ν takes the value $\nu = 0.154$ with the above choices of $\alpha = 0.39$, $t_p = 85$ fs, and $T = t_p / 10$.

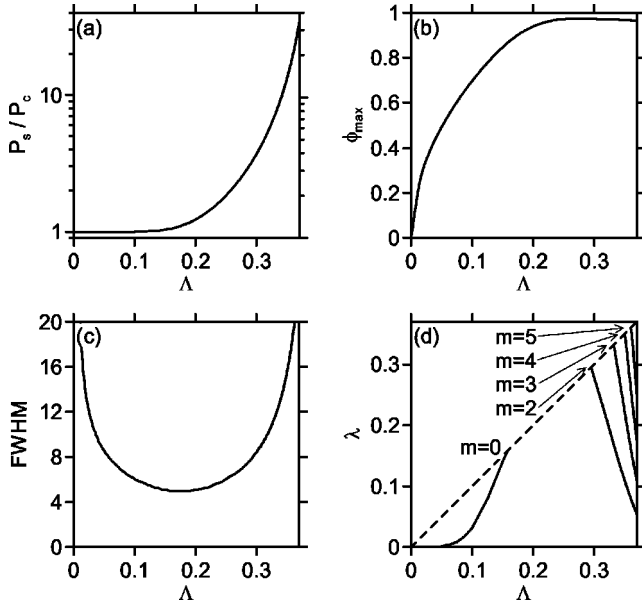


FIG. 1. (a) Soliton power vs Λ , (b) soliton amplitude vs Λ , (c) soliton width vs Λ , and (d) eigenvalues of the internal modes $\delta\phi$ vs Λ . The dashed line marks the maximum value of λ for which discrete (localized) perturbative modes exist, i.e., $\lambda \leq \Lambda$.

I. Conservative case $\nu=0$

In the nondissipative regime ($\nu=0$), Eq. (4) admits soliton solutions in the form $A = \phi(X, Y)\exp(i\Lambda Z)$, where the soliton shape ϕ is real-valued and satisfies

$$-\Lambda\phi + \Delta_{\perp}\phi + \phi^3 - \phi^{K+1} = 0. \quad (5)$$

Here, we restrict ourselves to the single-hump, nodeless ground state soliton solution. Figures 1(a)–1(c) show the basic properties of this soliton family characterized by P_s , i.e., the power $P = \int |A|^2 d\vec{R}$ computed on the shape ϕ , its maximum amplitude ϕ_{\max} and full width at half-maximum (FWHM) over the soliton parameter Λ . Low-power solitons are close to the Townes mode of the cubic NLS equation [corresponding to $|A|^2 \gg |A|^{2K}$ in Eq. (4)], with power $P_c = 11.68$ and near-Gaussian spatial shape [19]. High-power ones exhibit a shape resembling high-order super-Gaussians (SG). Their respective intensity ϕ_{\max}^2 is always below (although close to) the saturation threshold $I_{\max} = 1$.

An important feature is the monotonous increase of P_s vs Λ , which implies orbital stability of these nonlinear objects, in accordance with the so-called Vakhitov-Kolokolov criterion $dP_s/d\Lambda > 0$ [20] (see also Refs. [21–23]). Figure 1(d) confirms the stability of such stationary-wave structures from a numerical computation of azimuthal perturbations $\delta\phi \sim e^{im\theta + i\lambda Z}$ acting against the ground state ϕ , with angular number m and eigenvalue λ (see details on the related spectral problem in Appendix A). First, we observe that all eigenvalues λ are real-valued, so this family of solitons is linearly stable. Second, in the parameter range $0.16 < \lambda < 0.29$ ($1.05 < P_s/P_c < 3.2$ respectively) there are no internal modes, i.e., breather modes characterized by periodic oscillations in their amplitude. Therefore, in this regime we expect the solitons to be particularly robust due to the lack of internal os-

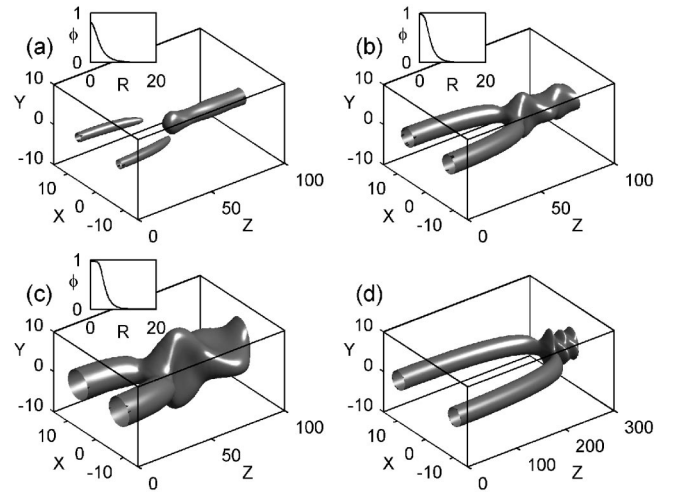


FIG. 2. Isointensity plots [$I_{\text{iso}}=0.5$] of the fusion of conservative solitons ($\nu=0$) with individual power P_{fil} and separation distance Δ . The insets show the radial shape of the respective soliton. (a) $P_{\text{fil}} = 1.02P_c$ ($\Lambda=0.137$) and $\Delta=15$. (b) $P_{\text{fil}} = 1.92P_c$ ($\Lambda=0.254$) and $\Delta=15$. (c) $P_{\text{fil}} = 3.84P_c$ ($\Lambda=3.02$) and $\Delta=15$. (d) Same parameters as in (b), but with $\Delta=20$.

cillations. The corresponding FWHM and intensity maxima expressed in physical units are 150–200 μm and $(5\text{--}7) \times 10^{13} \text{ W/cm}^2$, which is in excellent agreement with the usual waist and intensities reached by femtosecond filaments in air [16,17,24].

Solitons are strong nonlinear attractors. Starting with any low intensity field distribution containing sufficient power, self-focusing always leads to the formation of one or more solitons. Another consequence of this dynamics is that these objects attract each other and can mutually fuse. Figure 2 shows iso-intensity plots of the merging of two identical solitons with individual power P_{fil} and separation distance Δ .

From the above analysis, we expect solitons with powers $1.05 < P_{\text{fil}}/P_c < 3.2$ to be specifically robust (absence of internal modes). Indeed, for fixed $\Delta=15$, solitons without internal modes [Fig. 2(b)] merge at larger distances Z than those capable of internal oscillations [Figs. 2(a) and 2(c)]. Moreover, if we look at the final states after the fusion processes, only in Fig. 2(a) a robust, new fused static waveguide emerges, starting from $2P_{\text{fil}}/P_c \approx 2 < 3.2$. In Figs. 2(b) and 2(c), the opposite condition $2P_{\text{fil}}/P_c > 3.2$ leads to “breathing” solutions due to the internal mode with $m=2$. For an increased separation, $\Delta=20$, the point of fusion shifts to significant higher values of Z [Fig. 2(d)]. Reexpressed in physical units, two filaments separated from each other by a distance $\sim 0.6 \text{ mm}$ can propagate over more than 3 m before merging.

Using virial arguments detailed in Appendix B, these behaviors can receive a theoretical justification. Two Gaussian-like filaments (which is a reasonable approximation for $P_{\text{fil}} < 3P_c$) with an amplitude close to saturation may merge even without dissipation, provided that both their individual powers and mutual separation distance are below some thresholds. Whenever $\nu=0$, this property can indeed be anticipated from the dynamical relation governing the mean-square radius of the beam, $\langle R^2 \rangle = \int R^2 |\phi|^2 d\vec{R} / P$. Analyzing

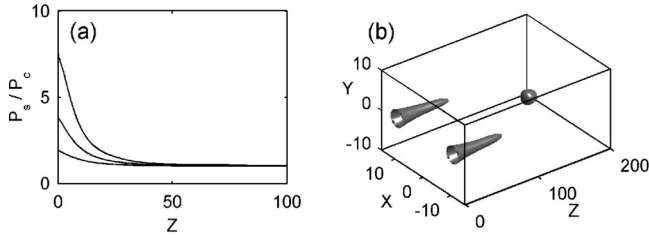


FIG. 3. (a) Decrease of soliton power P_s vs Z , $\nu=0.154$, for solitons with $P_s=1.92P_c$ ($\Lambda=0.254$), $P_s=3.84P_c$ ($\Lambda=3.02$), and $P_s=7.56P_c$ ($\Lambda=3.32$). (b) Same as in Fig. 2(d), but with $\nu=0.154$. In the region $100 < z < 150$ preceding the fusion event, beam components slightly diffract with an intensity going below the selected isointensity level [$I_{\text{iso}}=0.5$].

specific regimes for which the interaction terms entering the dynamical relation for $\langle R^2 \rangle$ remain relevant while the overall radius of the two-component beam decreases, it is found that merging applies in particular to Gaussian-shaped solitons with waist W_{fil} and power P_{fil} satisfying $\Delta \leq \Delta_{\text{lim}} = \sqrt{10} W_{\text{fil}}$ and $P_{\text{fil}} \leq 1.35P_c$. For wider separation distances ($\Delta \gg \Delta_{\text{lim}}$), the interaction terms vanish and the solitons should in principle cease to interact. Up to discrepancies linked to the starting assumptions (see Appendix B), these expectations are compatible with the results shown in Fig. 2.

2. Dissipative case $\nu \neq 0$

When MPA is introduced, Eq. (4) no longer admits stationary solutions. Nevertheless, especially for $\nu \ll 1$, the system still holds certain features, deducible from the conservative case. First, for intensities far below the threshold ~ 1 , the dissipative term is irrelevant anyway. So, in the self-focusing regime, formation of “solitons” can proceed as without losses. After reaching a “quasi-soliton” state with an intensity ~ 1 , dissipation comes into play. Since there exists a conservative ground state for all $P_s \geq P_c$, the “quasi-soliton” slides “adiabatically” down the curve in Fig. 1(a) until reaching the effective collapse threshold P_c of the cubic Schrödinger equation. Figure 3(a) shows this property for different powers of the initial soliton. Due to their “flat top” shape, high-power ground states undergo higher losses. As a consequence, starting with high power does not significantly enlarge the dissipation range, which was found numerically < 70 for input powers up to $20P_c$. Reexpressed in physical units using the above parameters α , t_p , and T , this value predicts a maximum filament length < 1 m per pulse, which agrees with the short “life-time” along z of the recurrent filaments observed in [13].

Modeling the solitons ϕ close to the saturation threshold as $\phi = \exp[-(R/W_{\text{fil}})^{2N}]$ with $N \geq 1$, it is possible to solve approximately the power relation $d_z P \approx -2\nu \int \phi^{2K} d\vec{R}$. By using $\int \phi^{2K} d\vec{R} = K^{-1/N} \int \phi^2 d\vec{R} \approx K^{-1/N} P_s$, we can evaluate the dissipation range ΔZ_{MPA} , along which the beam power persists above P_c , as

$$\Delta Z_{\text{MPA}} = \frac{K^{1/N}}{2\nu} (1 - P_c/P_s), \quad (6)$$

where P_s is the initial soliton power. This estimate takes the maximum value $\Delta Z_{\text{MPA}} \approx 25$ when $P_s \gg P_c$ and $N \rightarrow 1$. In

physical units, Δz_{MPA} predicts a maximum filament length of ≈ 0.35 m, which is in the same order of magnitude as our numerical result.

Last but not least, dissipation has a significant influence on the fusion dynamics. By comparing Fig. 3(b) to Fig. 2(d), we see that the presence of MPA promotes the mutual coalescence of filaments. The point of fusion shifts to significantly smaller propagation distances. This behavior is understandable in the sense that MPA shifts the “quasi-solitons” to the low power regime $P_{\text{fil}} < 1.05P_c$, where we expect an easier merging. Another interesting point is that the dissipation range can be enlarged with the help of the fusion mechanism. The central beam, visible in Fig. 3(b) at $Z \approx 150$, indeed clearly exceeds the predicted dissipation range of a single filament.

In summary, Eq. (4) stresses that spatial solitons are the natural objects modeling self-guided femtosecond filaments in the transverse plane. Although their individual range of propagation may be limited to short distances < 1 m by MPA, their capability of merging at relatively low powers enables them to propagate over more extended ranges.

IV. (2D+1)- VERSUS (3D+1)-DIMENSIONAL NUMERICAL SIMULATIONS

In this section, we return to physical units and compare results of our reduced 2D model [Eq. (3)] with corresponding space-time resolved 3D simulations [Eq. (1)].

A. 2D simulations

Reframed in the present context, Fig. 4 illustrates filamentation patterns in the 2D approximation, for which different beams undergo random perturbations. Because realistic perturbations mostly differ from oscillatory modulations lined on the maximum MI growth rate [11], we opted, by comparison with antecedent experimental data [5,6], for an input anisotropic N th-order SG beam in the form $\psi = \sqrt{I_0} \exp[-(x^2 + 2y^2)^N / w_0^{2N}]$, perturbed at $z=0$ m by an isotropic 10% random noise in amplitude and multiplied by a 10% noisy Gaussian temporal profile ($t_p=85$ fs). The fluence distribution [$F = \int_{-\infty}^{+\infty} |\mathcal{E}(t)|^2 dt$] of the resulting beam is then employed as the input condition for the 2D model. Figure 4(a) shows the isointensity plots for a perturbed beam with $N=3/2$, $w_0=1$ mm, and $P_{\text{in}}=20.5P_c$. The beam first forms a ring giving rise to two filaments. These merge and reform during a transient stage before they refocus into a robust lobe at center. Intermittency in filament nucleation occurs in the early propagation stage over short ranges, which can be compared with the scenario of the optically turbulent light guide proposed in [13]. However, at larger distances, the filaments relax to a single one in the (x, y) plane. This waveform afterwards does not change until the Rayleigh length ($z \rightarrow 4$ m), beyond which it diffracts slowly. Filaments reach the maximum intensity $I_{\text{max}} \sim 7 \times 10^{13}$ W/cm² over distances $\sim \Delta z_{\text{MPA}} < 1$ m, but they asymptotically remain captured in longer soliton envelopes that locate “optical pillars” in the medium. Similar patterns of two main filaments fusing into one were observed to generically occur with different beam

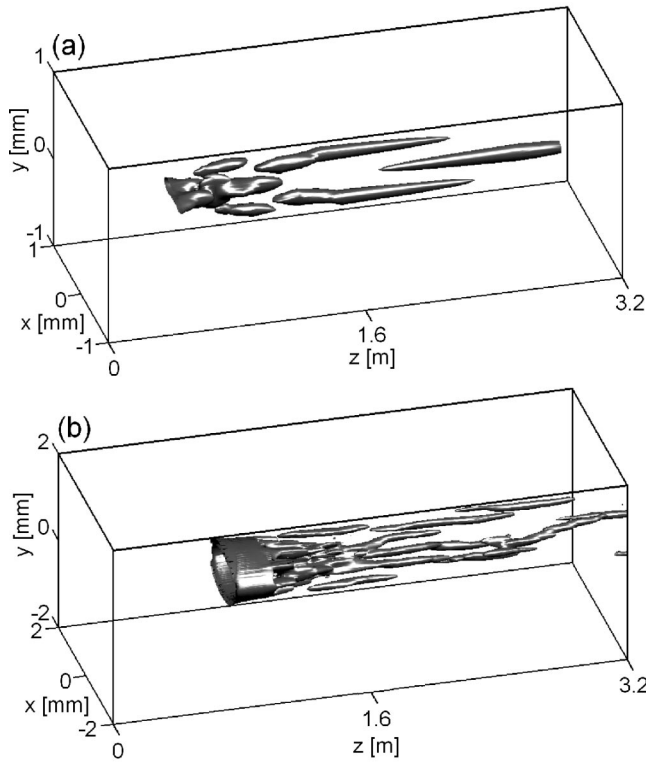


FIG. 4. Isointensity patterns ($I_{\text{iso}} \approx 10^{12}$ W/cm²) of filamentary structures described by Eq. (3) and created from a SG beam with (a) $N=3/2$, $P_{\text{in}}=20.5 P_{\text{cr}}$ and $w_0=1$ mm, and (b) $N=2$, $P_{\text{in}}=88 P_{\text{cr}}$ and $w_0=2$ mm.

shapes and peak powers comprised between $15P_{\text{cr}}$ and $40P_{\text{cr}}$. This dynamics fully agrees with previous experimental observations [5]. For higher powers, Fig. 4(b) shows a broader ($N=2$) SG beam with $88P_{\text{cr}}$ and wider waist $w_0=2$ mm. Filamentary structures with the largest separation distances create strong individual attractors which organize the beams into three major long-range pillars composed of solitonlike filaments. An early stage of “random nucleation” precedes the formation of these three filamentary channels, which may move in the (x, y) plane while they attempt to attain an equilibrium position.

Like the soliton pattern shown in Fig. 3(b), these two simulations confirm that the mutual interaction between optical cells helps in maintaining the robustness of the beam envelope over several meters.

B. 3D simulations

For comparison, Eqs. (1) are now solved by means of a spectral code using fast Fourier transforms in the (x, y, t) variables. Integration along the longitudinal axis (z) is performed with an adaptive step tuned on the intensity growth. In the transverse dimensions, a fixed mesh with $\Delta t \leq 0.5$ fs and $\Delta x = \Delta y \leq 15$ μm was used. Simulations were realized on the massively parallel machine (TERA) of the CEA, where we used up to 128 processors per run. Details on further numerical aspects and limitations in (3D+1)-dimensional computing are given in Appendix C.

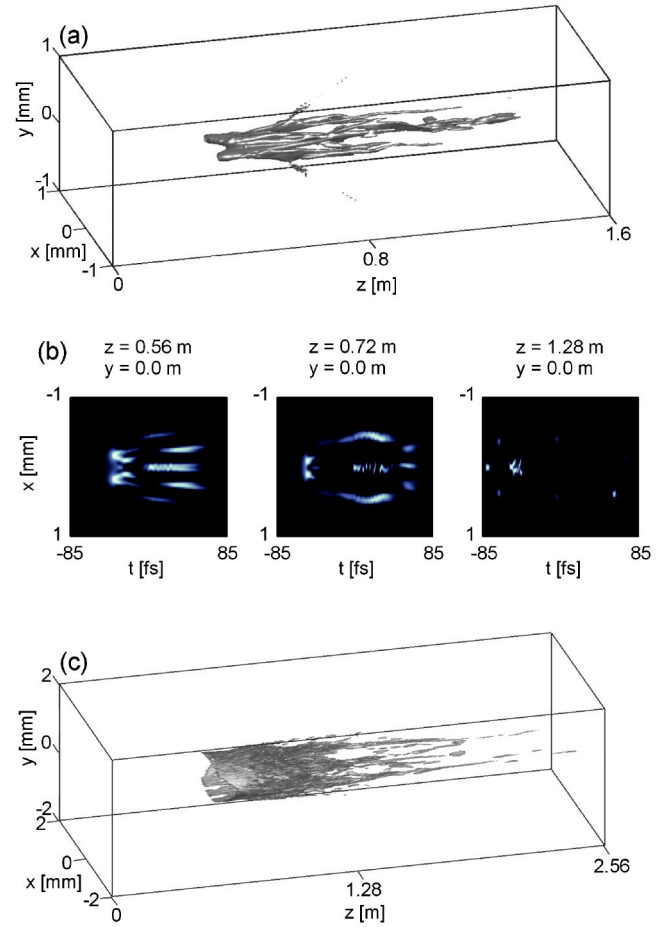


FIG. 5. (a) (Color online) Plasma strings [$\max_t \rho(x, y, z, t) \geq 10^{15}$ cm⁻³] of the $20.5P_{\text{cr}}$ SG beam used in Fig. 4(a). (b) $|\mathcal{E}|^2$ vs $(x, 0, t)$ for the same beam. (c) Plasma strings from the $88P_{\text{cr}}$ SG beam of Fig. 4(b).

Figure 5 shows the filamentation of pulses with the same input distributions as the ones used in Fig. 4. In Fig. 5(a) we display the plasma strings produced by the beam with $20.5P_{\text{cr}}$. Figure 5(b) shows their associated intensity profiles in the plane $(x, y=0, t)$ at different z positions, along the y axis crossing the two primary spots condemned to merge. The temporal pulse profile, even subject to strong distortions, does not prevent the transverse dynamics of the pulse from developing as in Fig. 4, up to second-order discrepancies in the focus point linked to the choice of T (see Sec. IV C). Although different temporal slices come into play, all of them support the propagation of cells first nucleated at different locations, then remaining localized around the *same* place in the (x, y) plane. Plasma strings associated with pulse components of maximum intensity and duration nearby $1/10$ of the input pulse dominate, which makes our previous assumption for averaging the (3D+1)-dimensional equations valid. Finally, Fig. 5(c) depicts the plasma strings created by the SG pulse with 88 critical powers, $N=2$ and $w_0=2$ mm. Three distinct channels clearly emerge in the (x, y) plane. They do not interact significantly but remain almost robust at their transverse position, in agreement with the filamentation pattern of Fig. 4(b).

C. Limitations of the reduced model

Major advantages in employing the 2D model concern, of course, the gain in computation time when we only focus on the spatial dynamics of the pulse (see Appendix C). With this aim, Eq. (3) has been successfully employed for clearing up alternative problems, such as, e.g., the interaction of an ultrashort filament with an opaque droplet [24,25]. Experiments on this topic [24] revealed the remarkable robustness of femtosecond filaments with typical waists $\sim 150 \mu\text{m}$ when they hit a micrometric droplet with a diameter as large as $2/3$ the filament size. The collision results in a minimal loss of energy and the filament self-heals over very short distances. Recent numerical investigations [25] analyzed this intriguing property. The interaction pattern, simulated from the full 3D system, displayed evidence of the complete rebuilding of the pulse over 2 cm only. The same filament modeled by solitons of Eq. (3) restored an identical pattern within the same longitudinal interval.

Besides such convenient aspects, a 2D reduction of the propagation equations cannot, unfortunately, avoid certain weaknesses. Identifying a 3D, time-resolved filament with a 2D “soliton” means that we only focus on the core of the filament and discard its different time slices [15]. Indeed, Eq. (3) accounts for the time slice with maximum intensity only. For describing, e.g., the self-healing of a fs filament with a micrometric droplet, this simplification has almost no incidence because the interaction length of the beam with the obstacle is short along the z axis. However, when we simulate long-range propagations, certain concessions in the agreement with fully time-resolved computations have to be made.

(i) The arbitrary choice of the temporal extent $T=0.1t_p$ prevents us from restoring quantitatively the early self-focusing distances of a beam at relatively low powers ($\leq 100P_{\text{cr}}$), as can be seen by comparing Figs. 4 and 5. Indeed, this choice determines the value of the parameter α [Eq. (3)] that fixes the effective critical power in the pulse time slice under consideration. Setting $T=0.1t_p$ is suitable for describing filamentation patterns evolving in ionization regimes, but this choice can lead to visible discrepancies in the location of the first focus point, for which the value $T=t_p$ yielding a higher α would be more adapted. Remembering Marburger’s formula [10] that evaluates the collapse point, z_c , of collimated Gaussian beams in the self-focusing regime:

$$z_c = \frac{0.367z_0}{\sqrt{(\sqrt{\alpha P_{\text{in}}/P_{\text{cr}}} - 0.852)^2 - 0.0219}}, \quad (7)$$

it is seen right away that the differences in the location of the self-focus point indeed become more pronounced at low ratios $P_{\text{in}}/P_{\text{cr}}$ and for low values of α .

(ii) Experimental setups for femtosecond pulse propagation are currently based on chirped-pulse amplification (CPA) Ti:sapphire laser sources. CPA techniques allow us to modify the effective initial pulse duration by varying the distance between the gratings of the pulse compression system. These variations also entail a chirp onto the input pulse phase ($\mathcal{E} \rightarrow \mathcal{E}e^{iCr^2}$, $C=\text{const}$), which can lead to noticeable changes in the early self-focusing distances by GVD com-

ensation [26]. Pulse chirping is used to monitor the onset of filamentation [14,27]. Since Eq. (3) ignores the temporal dynamics, applying this model to pulses with an initially large chirped phase may then enhance the differences with the experimental observations.

(iii) Because the averaging procedure involves a single time slice only, the 2D model cannot describe the second focusing of pulses (see, e.g., [16]), which characterizes femtosecond filaments and enables the latter to pursue their propagation over about 1 m. This second refocusing is associated with the late growth of the trailing edge of the pulse. Although it concerns a residual propagation interval in which the pulse intensity noticeably decreases, this process allows one to maintain a femtosecond filament over larger distances than those accessible by the reduced model. In connection with this point, the 2D model also overestimates the losses due to MPA. In full 3D configurations, defocused time slices with lower intensities can maintain a nearly constant power upon propagation until they may focus again. The reliability of the reduced model may thus be limited in, e.g., examining some postionization regimes.

The above discrepancies must not, however, elude the major advantage of the 2D model, which can describe the qualitative dynamics of ultrashort, high-power pulses with broad waists over considerable distances of propagation.

Keeping these limitations in mind, but aware of the information conveyed by the 2D model, we can outline, on the basis of the previous 2D and 3D numerical results, a generic scenario for the filamentation of terawatt fs pulses as follows: (i) Beam modulations give rise to short-range filaments that grow in intensity until reaching the ionization threshold I_{max} . In this limit, near-soliton filaments, searching for an equilibrium position, recur in the diffraction plane within an optically turbulent regime during the early stage of propagation [13]. (ii) As they attain a quasistable configuration with respect to their neighbors, short-range filaments either amalgamate or self-attract without merging, depending on their inner power and separation distances, in order to form a limited number of clusters, named as “optical pillars.” These optical pillars then continue the propagation over longer distances.

Note that this scenario applies to input beams where an isotropic random noise first creates short-scale cells that next relax to quasicohherent structures. For experimental beams exhibiting salient defects, it is not excluded that optical pillars are fixed by the most intense defects of the input beam profile, which further excite turbulent cells in their vicinity, as evidenced below (see also [7]).

V. LONG-DISTANCE PROPAGATION EXPERIMENTS

To figure out how terawatt laser pulses degenerate into multiple filaments over long distances, we investigate some evolution stages in the filamentation patterns produced by the Teramobile laser [14]. This laser system delivers at the 10-Hz rate pulses with energy up to 0.5 J, transverse diameter equal to 5 cm ($w_0 \approx 2.5$ cm), and FWHM duration tunable from 100 fs (minimal chirp) to 600 fs (large negative chirp) by detuning the compressor with a chirp opposite to

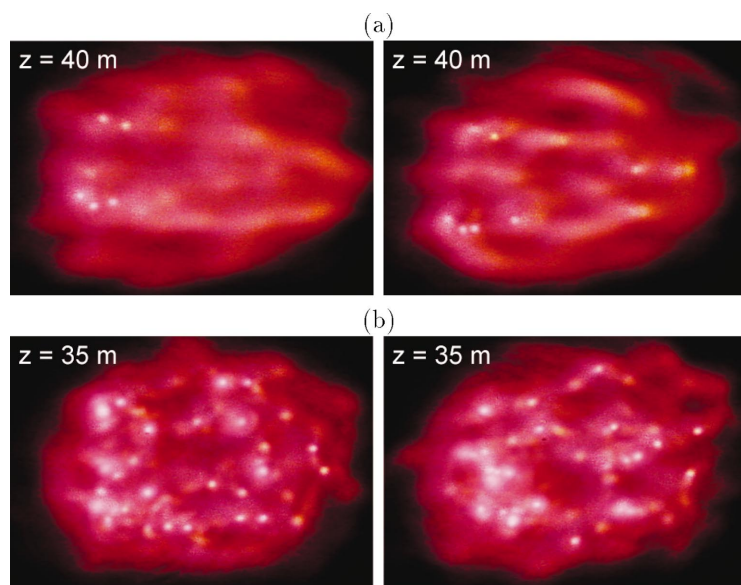


FIG. 6. (Color) Shot-to-shot fluctuations in the filamentation pattern of the 10-Hz rated Teramobile laser delivering 230-mJ pulses with (a) 600 fs duration ($P_{\text{in}} \approx 120P_{\text{cr}}$) at $z=40$ m, and (b) 100 fs duration ($P_{\text{in}} \approx 700P_{\text{cr}}$) at $z=35$ m.

air dispersion. The collected experimental data consist of photos taken from a white screen positioned in the plane orthogonal to the beam path. In the first two series of experiments (Figs. 6–8), a filter with narrow bandwidth around $\lambda_0=800$ nm was put in front of the camera. Two photos with exposure time of 1/8th s were taken at each distance, so that pictures mostly show single-shot beam patterns. Pictures featuring double-pulse images did not present qualitative change from shot to shot, up to slightly more visible filaments or more pronounced ones at certain distances (see Fig. 6). Although the number of “visible” filaments may vary to some extent, the zones at which distinct clusters of filaments develop remain identical and only the relative intensity of certain spots exhibit differences. We consider these fluctuations as being of second-order importance in the global evolution of the filamentation pattern.

Concerning this point, let us emphasize that the resemblance between the experimental and numerical patterns in the forthcoming analysis will not lie in the exact position and number of the filaments, which may undergo similar fluctuations and are subject to atmospheric turbulence or local diffusive processes as they propagate. Instead, qualitative similarities occur in the following sense: Starting with an input coarse profile, the beam amplifies its initial inhomogeneities and, through modulational instability, it produces bright spots connected by lower-intensity bridges. A “global” pattern then emerges from the zones of highest concentration of light, which create characteristic figures (ring/trident/cross). These aspects are actually well restored by the 2D simulations, using the digitized fluence of the experimental input beam.

A. “Low”-power filamentation regime

To start with, we examine the filamentation dynamics of terawatt beams with about 100 critical powers only. Figure 7 shows the occurrence of light filaments over 55 m from the Teramobile beam with 230 mJ energy and pulse duration of 600 fs. Modulations induced by caustics distributed in the

spatial beam profile develop as follows: In the early propagation stage, the broad (SG-like) beam tends to develop a ring-shaped zone by diffraction. At the edge of the beam where fluctuations are the most intense, filaments emerge from local defects. Next, several cells occur along a flattened ring inside the focal spot. More filaments are then generated around this ring. They finally self-organize into a three-pronged fork shape.

For comparison, we integrated the (2D+1)-dimensional Eq. (3) from a data file of the experimental input beam measured at the distance $d=1$ m after the laser exit. With a pulse duration of 600 fs ($t_p \approx 510$ fs), the coefficient α in Eq. (3) takes the value $\alpha=0.51$. With a beam waist of 2.5 cm, a very high spatial resolution [namely, 8192^2 in the (x,y) plane for a box length of $6w_0$] was required in order to solve narrow optical structures reaching 1000 times the input beam intensity I_0 . Figure 7(b) illustrates the results of numerical simulations. The beam containing ~ 120 critical powers begins to form local clots from the highest intensity regions. Then, others emerge along a ring inside the focal spot. The final pattern, involving several small-scale spots, results in a trident-shaped figure, comparable with the experimental one. For such beams with a few tens of critical powers only, Eq. (6) describes the filamentation of a disordered optical distribution having an effective ratio of input power over critical of about $\sim \alpha P_{\text{in}}/P_{\text{cr}} \approx 60$, which limits at the very most to $P_{\text{in}}/P_{\text{fil}} \approx 24$ the number of genuine filaments reaching the ionization threshold. Filaments develop as asymptotic states and become decoupled from the initial amplitude and phase of the wave field. The discrepancy existing in the distance where the first filaments occur, $z_c \approx 50$ m, and the experimental measurement, $z_c \approx 30$ m, is attributed to the pulse chirping, which Eq. (3) ignores, and to our former choice $T=0.1 t_p$. As underlined in Sec. IV C, this value suits the experimental development of filaments in the ionization regime, but it cannot restore the early self-focusing distances of the beam requiring rather $T=t_p$. Keeping $T \ll t_p$ is, however, necessary to approach a suitable averaged power ratio in the ionization regime, where filaments mostly evolve.

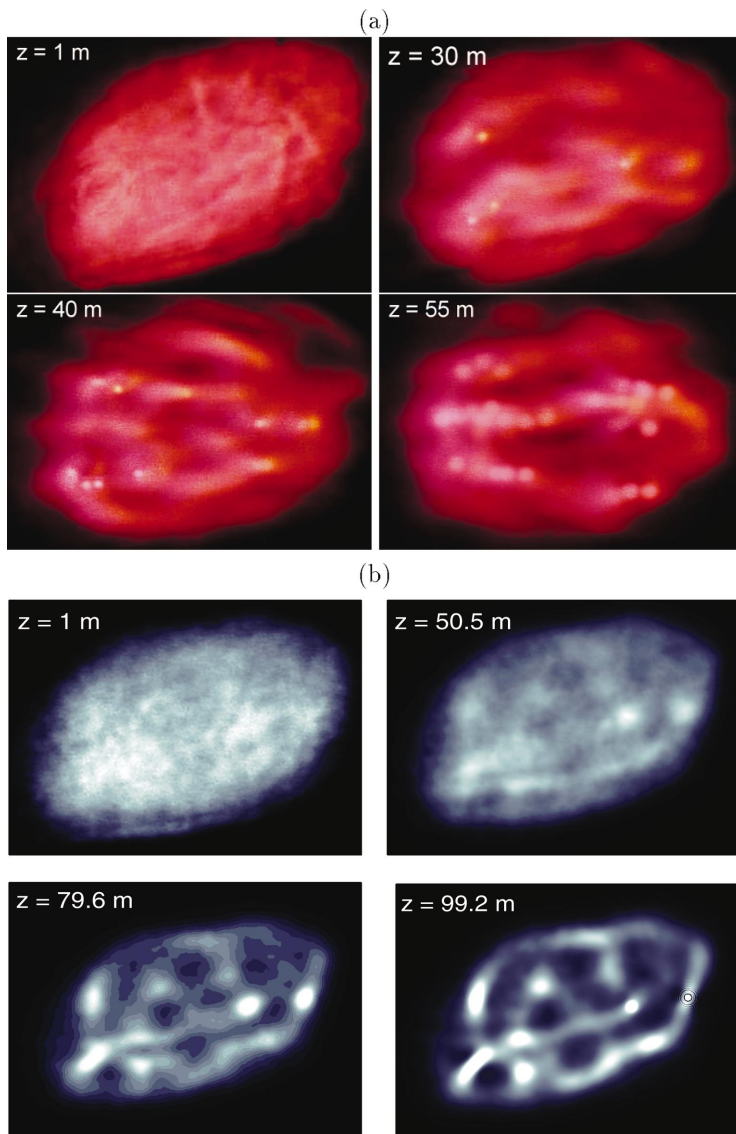


FIG. 7. (Color) Filamentation patterns (a) produced experimentally for the $120 P_{cr}$ beam at $z = 1, 30, 40,$ and 55 m. (b) Numerical computations of the same beam from Eq. (3). Maximum intensity is limited to twice the input intensity. In this figure as well as in Figs. 8 and 9, the image scale is about $1.5 w_0 \times 1.5 w_0$ ($w_0 =$ input beam waist), for both the experimental and numerical snapshots.

From the numerical as well as experimental patterns, we can observe that some filamentary channels persist from the first focus point over several meters, whereas others are randomly nucleated over shorter longitudinal scales.

B. “Moderate”-power filamentation regimes

Reducing the pulse duration to 100 fs ($t_p = 85$ fs) makes it possible to investigate filamentary patterns promoted by fs beams with powers as high as $700 P_{cr}$, i.e., 2.3 TW. In this case, displayed in Fig. 8(a), the beam breaks up into more cells than in the previous lower-power case. Following the estimate recalled in the Introduction, up to $\alpha P_{in}/P_{fil} \sim 110$ light cells may form in principle with $P_{fil} \approx \pi^2 P_{cr}/4$. Figure 8(b) reproduces these experimental patterns from a numerical integration of Eq. (3) performed with the parameter $\alpha = 0.39$ fixed by $t_p = 85$ fs. Note that the discrepancies in the early self-focusing distances signaled in the previous case almost completely disappear at higher powers. Here, a minimal pulse chirping was used. The agreement between the experimental and numerical results is thus quite satisfactory.

The labels (1)–(3) locate active zones in the beam, which can clearly be identified in both the experimental and numerical patterns: (1) points out a couple of bright, robust filaments, (2) restores an arch of the diffraction ring pattern supporting primary hot spots while (3) indicates a crosswise configuration of filaments. By comparing the four snapshots with those displayed in Fig. 7, these patterns reveal that, although some filaments are able to survive over several meters at the most powerful regions of the pulse, random nucleation of filaments in the entire focal spot seems more privileged, compared with the break-up of the former $120 P_{cr}$ beam. We explain this property by the high power density. “Optical pillars” cannot propagate independently due to their smaller separation distance. The primary filamentary cells experience more substantial power transfers through the overall surface of the beam.

C. “High”-power filamentation regimes

Concerning now higher power levels, Fig. 9(a) displays filamentation stages for pulses delivered by the Teramobile

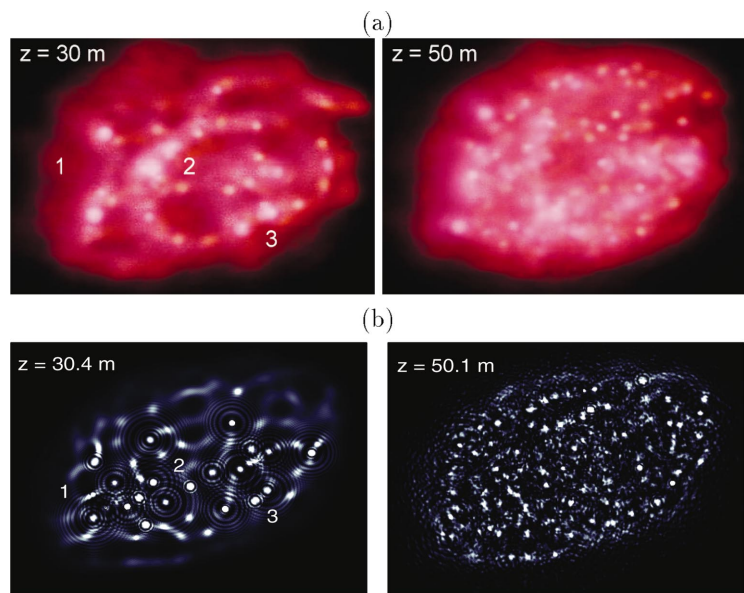


FIG. 8. (Color) Filamentation patterns (a) produced experimentally for the $700 P_{cr}$ beam at $z = 30$ and 50 m. (b) Numerical computations of the same beam from Eq. (3). Labels (1)–(3) indicate beam zones discussed in the text.

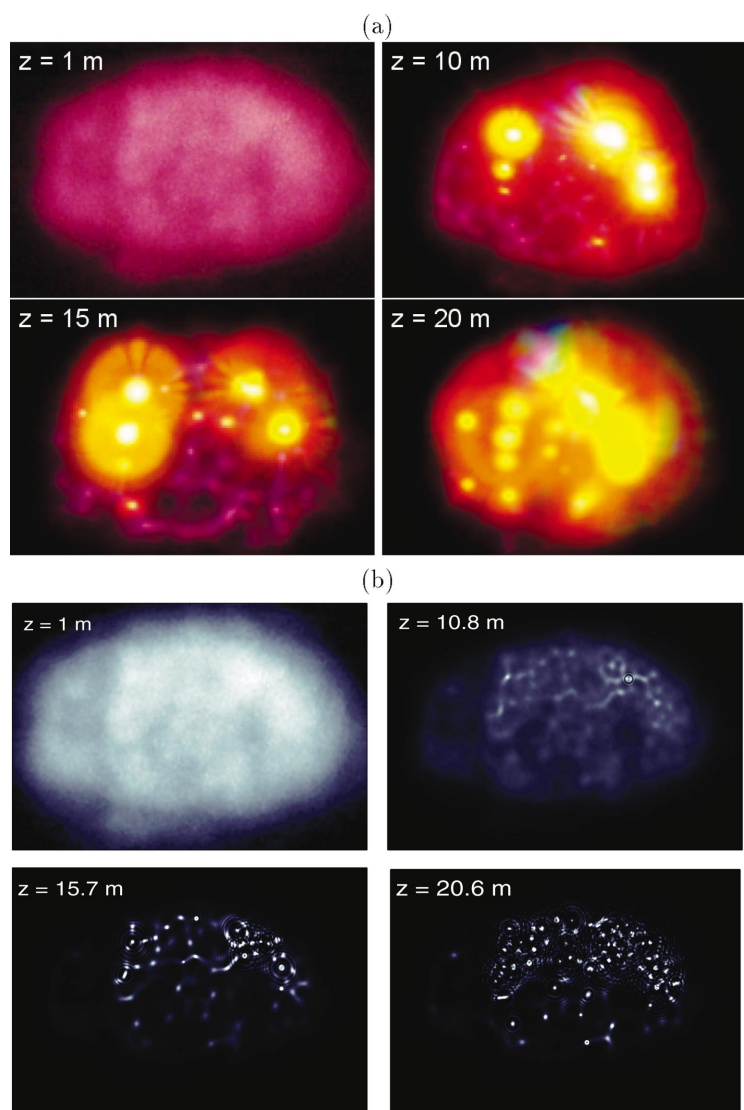


FIG. 9. (Color) Filamentation patterns of the $1000 P_{cr}$ beam delivered by the Teramobile at different propagation distances: (a) Experimental transverse distributions. (b) Image plots from numerical computations performed with Eq. (3).

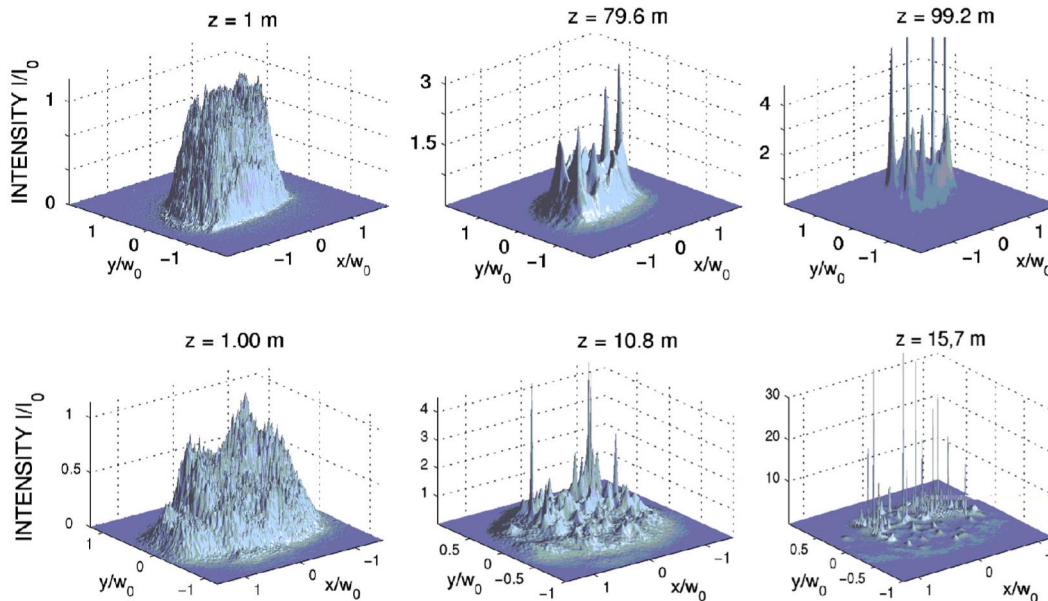


FIG. 10. (Color online) Intensity vs (x,y) for the beams shown in Fig. 7(b) (top row) and Fig. 9(b) (bottom row).

system, with a FWHM duration of 100 fs ($t_p=85$ fs) and 330 mJ energy. The power range thus accesses 3 to 4 TW, i.e., about 1000 critical powers. No filter was used in this series of experiments. Although a nontrivial level of overexposure cannot be avoided from the most intense regions of the beam, removing the 800 nm filter makes it possible to exhibit true-colored filaments and to emphasize major optical pillars through the white-light conical emission which signals the presence of nonlinear self-focusing and subsequent plasma generation [14,27]. The filamentation scenario follows the former one: A ring-shaped zone supports a few big spots initiated by the highest-intense defects of the input beam. These “hot” spots self-focus more and more over several tens of meters, while white light occurs on the detection screen. MPA dissipation and evacuation of power excess due to the collapse dynamics undergone by the primary filaments allows one to transfer power to the central zone of the beam, which serves as an energy reservoir for exciting secondary filaments. Equation (3) computed with $\alpha=0.39$ ($t_p=85$ fs) restores these features with almost no discrepancy in the first focus point [$z_c \approx 10$ m], as the beam contains very higher power. Figure 9(b) reproduces the experimental images in the same longitudinal interval.

From the numerical computation, the bright spots observed in the experiments appear to be first excited by an intense primary filament, which afterwards give rise to a bunch of secondary ones emerging as smaller-scale cells located near the central spot. We can observe how the local defects rapidly generate intense spots along a ring. In the upper arch of this ring, the most intense filaments, either as individual entities or gathered in clusters of a few cells, produce ~ 4 distinct active zones, in agreement with Fig. 9(a). These zones actually consist of robust optical pillars, following the definition given above. They persist over several tens of meters, whereas secondary filaments rapidly recur first around them, and next in the central part of the beam.

Figure 10 details the spatial distortions undergone by the

lowest ($120 P_{cr}$, top row) and highest ($1000 P_{cr}$, bottom row) power beams, computed with the 2D reduced model. It displays evidence in both cases of the early amplification of the initial beam defects, which serve as central spots around which short-living filaments develop into an optical pillar. Note the growth of intense spikes that remain in a self-focused state over several tens of meters, while secondary peaks attain similar intensities at later distances.

D. “Moderate”-power beams in focused geometry

While the previous observations on screens provided detailed information about the beam structure at a given distance, they were, however, limited to semiquantitative observations. Fluctuations in the initial beam as well as from the atmosphere let the profile vary from shot to shot (see Fig. 6), so that successive images at different distances cannot be taken as quantitative information providing a complete propagation sequence over long distances. Moreover, the continuity and length of the individual filaments could not be assessed with accuracy.

In order to circumvent this limitation, we used a spatially extended, single shot characterization of the beam profile. The Teramobile laser was slightly focused ($f=40$ m) from a larger beam waist ($w_0 \approx 5$ cm) and emitted an energy of 250 mJ in 100 fs pulses (2.5 TW, $760 P_{cr}$). It was installed outdoors on flat humid ground and shot against the wind direction into an aerosol generator producing a thin haze at a distance of 48 m from the laser exit. With a soft regular wind, this setup produced a pretty homogeneous light haze along a distance of up to 10 m towards the laser beam. The haze density was adjusted so that beam scattering was efficient enough to detect the filaments, with limited perturbation on the beam propagation itself. In those conditions, image blurring by multiple scattering was negligible [24].

The beam was imaged with a CCD camera in true colors, from a near-forward direction. More precisely, the CCD

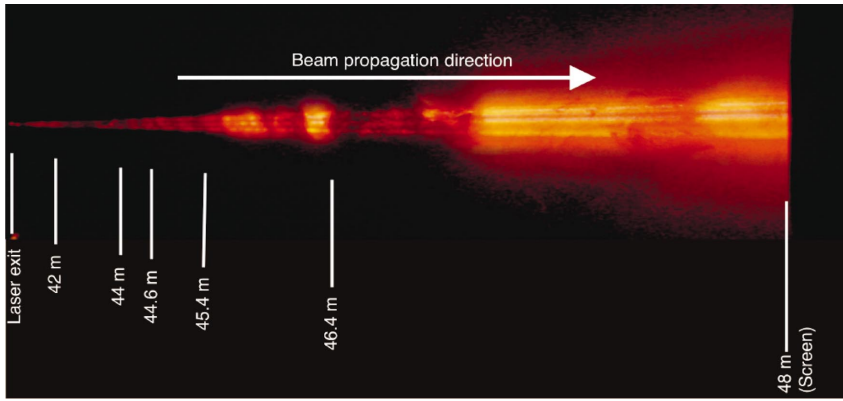


FIG. 11. (Color) Three “robust” filamentary structures propagating over ~ 8 m from the focal point ($f \approx 40$ m) of a converging beam with $760 P_{cr}$ delivered by the Teramobile laser system.

camera was placed over the aerosol generator, about 25 cm above the center of the laser beam, and directed to the laser output of the Teramobile system. This setup allowed us to acquire single shot (exposure time 1/8 s) pictures of a long section (up to 10 m) of the beam (Fig. 11). Triangulation, calibrated with reference points along the laser path, enabled us to retrieve the distance calibration indicated in Fig. 11. Note that the beam was imaged with a very strong parallax, since the camera was placed at only 25 cm above it. Hence the triangulation yielding the distance scale is not linear and explains the apparent short distance between the laser exit and the first marked distance (42 m).

Figure 11 exhibits a quasicontinuous three-pillar structure that emerges from $z > 40$ m and was reproducible from image to image. In this figure, the fluctuating intensity along the beam path is due to inhomogeneities in the haze, as was checked by visual inspection. Here, the observation of seemingly continuous structures along several meters on a single-shot image is evidence for the occurrence of optical pillars within femtosecond laser beams. In the present configuration, the beam self-organizes into three major, distinct clusters of light after passing through the focal point of the long-range converging lens.

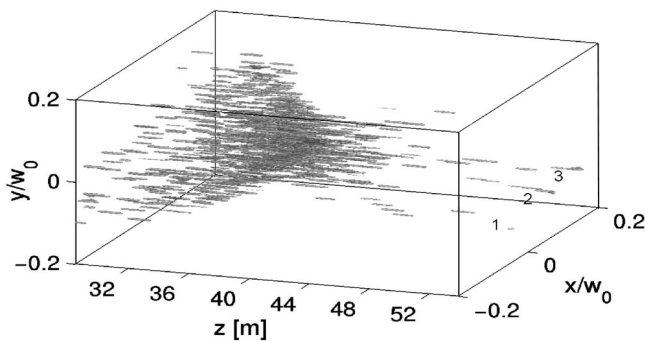


FIG. 12. Propagation of the same beam as in Fig. 11, numerically computed from Eq. (3) with a digitized data file of the input beam intensity profile affected by a spatially parabolic phase. Three filaments, identified by the labels 1, 2, and 3, can develop long sequences (≥ 2 m) after the focus. Although partly disconnected over ~ 10 m, their strong directivity yields the appearance of quasicontinuous strings of light. The numerous filaments occurring at $z < 40$ m are not visible in Fig. 11 due to the strong parallax in the beam imaging.

Figure 12 shows a 3D plot issued from a direct numerical integration of Eq. (3), using the same input intensity distribution multiplied by the parabolic phase $e^{-ik_0 r^2/2f}$ that accounts for the lens curvature ($f=40$ m). As seen from this figure, many filaments arise as the beam approaches the focal length $z \approx f=40$ m, where its minimum waist is attained. Remarkably, few filamentary structures emerge after this point: Only three of them propagate over ~ 10 m, under the form of sequences of quasicontinuous channels having the same direction and capable of covering more than 2 m as a whole. We attribute the transverse deflection of the most external filaments to the natural divergence of the beam envelope after the focus. This result again confirms the validity of the (2D+1)-dimensional model, together with the concept of “optical pillars”: Long-range filaments can develop as individual entities located in the same region of the transverse plane, where a few intense cells are recurrently emitted as they propagate in a quasicontinuous way.

VI. CONCLUSION

In summary, we have investigated the multiple filamentation of infrared femtosecond pulses in air, engaging high powers in parallel and focused geometries. Although intermittency of filaments affects the pulse dynamics, turbulent cells can converge towards long-range envelopes. These maintain the propagation over long distances while keeping an intensity close to the ionization threshold.

To understand these behaviors, we elaborated on a 2D model [Eq. (3)] describing the spatial dynamics of fs pulses, even when they undergo a delayed Kerr response. First, we thoroughly discussed the major properties of this reduced model by specifying both conservative and dissipative fundamental solitonlike solutions and their mutual interaction regimes. A noticeable enhancement of the propagation range through fusion processes combined with MPA was put in evidence. Second, we tested this model over a few meters for ultrashort mm-waisted pulses. By fixing the effective pulse temporal extent T to 1/10 of the input duration in ionization regimes, results from this simplified model were observed to reasonably agree with the transverse patterns of (3D+1)-dimensional pulses. For narrow beams ($w_0=1$ mm) and weak powers ($\leq 40P_{cr}$), two filaments form and merge into one central lobe. For broader beams ($w_0=2$ mm) up to

90 P_{cr} , several filaments propagate almost independently of their neighbors. The physical length of each asymptotic filament is of the same order (≤ 1 m) in both configurations. This result is important, since Eq. (3) provides an easy model to integrate, which can be useful for estimating the number and position of filamentary channels created by high-power fs pulses.

Next, we investigated experimentally the multiple filamentation of collimated beams delivered by the Teramobile laser, for powers up to 3 to 4 TW. Experimental patterns were then simulated by means of the previous 2D reduced equation, using a digitized file of the input beam fluence as an initial datum. Along distances limited to 100 m, long-range filaments were observed to be initiated by the most intense fluctuations of the input beam and those may persist over several tens of meters. From these “optical pillars,” small-scale spots arise and recur rapidly at other places in the diffraction pattern, in agreement with the scenario of “optically-turbulent light guides” proposed in Ref. [13]. The long-living primary filaments, as well as unstable randomly nucleated ones, can be described by the 2D model, which reproduces the qualitative behaviors in the filamentation patterns. Direct confrontations of terawatt ultrashort pulses and their numerical simulations revealed the existence of active optical zones keeping the beam collimated over considerable distances.

Finally, focused beams were investigated over several tens of meters along a complete propagation sequence. By optical coalescence, reduction of the beam waist in linearly focused geometry allowed us to form very long light channels over almost 10 m by gathering all filamentary components into a limited number of light strings. These strings, although longer than one elementary filament and keeping the same direction, were numerically revealed to still develop from intermittent cells remaining localized in the same region of the diffraction plane. This observation thereby confirms the concept of “optical pillars” supporting the long propagation of quasicontinuous light tubes.

ACKNOWLEDGMENTS

The authors thank Dr. S. Champeaux for preliminary works during a stay at Jena University and Cl. Gouédard for preparing data files of the experimental input beams. L.B. thanks Dr. M. Kolesik from Tucson University for fruitful discussions. Experiments were performed in the framework of the Teramobile project, funded jointly by CNRS and DFG.

APPENDIX A: SPECTRAL PROBLEM FOR SOLITON STABILITY AGAINST NONISOTROPIC PERTURBATIONS

We briefly sketch the spectral equations for the ground state stability versus nonisotropic perturbations with azimuthal number m . According to the standard procedure for linear stability analysis we introduce a small perturbation $\delta\phi$ on the soliton shape ϕ . We plug $A = (\phi + \delta\phi)\exp(i\Lambda Z)$ into Eq. (4) and linearize it with respect to the perturbation. The resulting evolution equation for the perturbative mode $\delta\phi$ is then given by

$$\frac{\partial}{\partial Z}\delta\phi = i\Delta_{\perp}\delta\phi - i\Lambda\delta\phi + i2\phi^2\delta\phi + i\phi^2\delta\phi^* - i(K+1)\phi^{2K}\delta\phi - iK\phi^{2K}\delta\phi^*. \quad (A1)$$

In order to separate azimuthal eigenfunctions of the transverse Laplacian, we transform Eq. (A1) from Cartesian (X, Y) to polar (R, Θ) coordinates. With the ansatz $\delta\phi(R, \Theta, Z) = \delta\phi_1(R)\exp(im\Theta + i\lambda Z) + \delta\phi_2^*(R)\exp(-im\Theta - i\lambda^*Z)$, the eigenvalue problem is then derived under the form:

$$\begin{pmatrix} \hat{L}_{11} & \hat{L}_{12} \\ \hat{L}_{21} & \hat{L}_{22} \end{pmatrix} \begin{pmatrix} \delta\phi_1 \\ \delta\phi_2 \end{pmatrix} = \lambda \begin{pmatrix} \delta\phi_1 \\ \delta\phi_2 \end{pmatrix}, \quad (A2)$$

where $\delta\phi_1$ and $\delta\phi_2$ are independent complex functions, $\hat{L}_{11} = -\hat{L}_{22} = \Delta_{\perp} - \Lambda + 2\phi^2 - (K+1)\phi^{2K}$ and $\hat{L}_{12} = -\hat{L}_{21} = \phi^2 - K\phi^{2K}$.

Figure 1(d) in Sec. III B shows the eigenvalues λ of the discrete (localized) perturbation modes $(\delta\phi_1, \delta\phi_2)$ of Eq. (A2), numerically identified for different values of m . All modes have zero growth rate ($\text{Im } \lambda = 0$), which implies linear stability.

APPENDIX B: VIRIAL ARGUMENTS FOR THE FUSION OF CONSERVATIVE SOLITONS

By repeating the analysis proposed in [11], the merging of nonlinear filaments follows from the dynamical relation governing the mean-square radius of the beam, $\langle R^2 \rangle = \int R^2 |\phi|^2 d\vec{R} / P$, whenever $\nu = 0$:

$$P d_Z^2 \langle R^2 \rangle = 8 \int |\nabla_{\perp} A|^2 d\vec{R} - 4 \int |A|^4 d\vec{R} + \frac{8K}{K+1} \int |A|^{2(K+1)} d\vec{R}, \quad (B1)$$

and applied to two Gaussianlike solitons with waist W_{fil} , power P_{fil} , and intensity close to saturation. After inserting the two-component trial solution

$$A_{\text{in}} = \sqrt{\frac{2P_{\text{fil}}}{\pi W_{\text{fil}}^2}} \left[e^{-|\vec{R} + \vec{\Delta}/2|^2 / W_{\text{fil}}^2} + e^{-|\vec{R} - \vec{\Delta}/2|^2 / W_{\text{fil}}^2} \right],$$

expanding Eq. (B1) enables us to predict that well-separated filaments ($\Delta > \sqrt{2}W_{\text{fil}}$) should fuse into a single lobe if the total beam radius decreases in self-compression regimes ($d_Z^2 \langle R^2 \rangle < 0$) where the exponentially decreasing interaction terms remain dominant. When the beamlet intensities attain their saturation level ($2P_{\text{fil}} / \pi W_{\text{fil}}^2 \rightarrow 1$), Eq. (B1) reduces to the interplay between linear (\mathcal{F}_{lin}) and nonlinear (\mathcal{F}_{nl}) contributions, i.e., $P d_Z^2 \langle R^2 \rangle \approx (32P_{\text{fil}} / W_{\text{fil}}^2)(\mathcal{F}_{\text{lin}} - \mathcal{F}_{\text{nl}})$ with

$$\mathcal{F}_{\text{lin}} = 1 + (1 - X)e^{-X}, \quad (B2)$$

$$\mathcal{F}_{\text{nl}} = 0.93 \frac{P_{\text{fil}}}{P_c} \left[1 + 3e^{-2X} + 4e^{-3X/2} - \frac{2K}{(K+1)^2} \times [1 + 2(K+1)e^{-(2K+1)X/(K+1)}] \right],$$

where $X \equiv \Delta^2 / 2W_{\text{fil}}^2$. The requirement that interaction terms

dominate (mostly through linear diffraction in \mathcal{F}_{lin}) while the beam still self-compresses imposes certain constraints on the power level, which must not be too high for avoiding strong localization of the solitons at their own centroids. This need particularly applies to Gaussian-shaped solitons satisfying $\Delta \leq \Delta_{\text{lim}} = \sqrt{10} W_{\text{fil}}$ and $P_{\text{fil}} \leq 1.35 P_c$. For wider separation distances ($\Delta \gg \Delta_{\text{lim}}$), exponential terms in Eq. (B2) vanish and the solitons are expected to no longer interact mutually.

These predictions reasonably agree with the results of Fig. 2. Note, nonetheless, that the previous restrictions inferred on the power bounds and separation distances are subject to discrepancies linked to the modeling of soliton shapes by Gaussian functions with saturated intensities. Figure 2(d) shows, for instance, that solitons with powers exceeding $1.35 P_c$ and separation distances $\Delta > \Delta_{\text{lim}}$ ($\Delta_{\text{lim}} \approx 15$) are still able to merge at long propagation distances. However, those distances are large compared with the dissipation ranges limiting the filament self-guiding when we introduce $\nu \neq 0$ (see Fig. 3).

APPENDIX C: COMPLEMENTARY NUMERICAL ASPECTS

In this appendix we shortly discuss some specifications related to our numerical codes. A spectral split-step scheme was employed for solving Eqs. (1) and (3). Fast Fourier transformations were performed along the space-time directions (x, y, t) by routines of the FFTW library, version 3. All codes were parallelized for distributed memory architecture by using the MPI (message passing interface) library. Throughout the simulation, the increment along the z axis adapted itself as a function of the wave field intensity computed from the nonlinear phase variations, i.e., $\Delta z / 4z_0 < a I_0 / I_{\text{max}}$ with a remaining weaker than 10^{-3} . Relaxation to larger steps Δz was monitored by an upper limit $\Delta z / 4z_0 > b I_0 / I_{\text{max}}$ with $b \geq a / 2.5$. Absorbing boundary conditions and a sufficiently large numerical box with characteristic lengths $L_t \geq 6t_p$, $L_x, L_y \geq 6w_0$ guaranteed an undisturbed propagation of the pulse. The number of points required for an adequate resolution currently attained 512–1024 in space and 2048 in the temporal direction for the (3D+1)-dimensional numerical runs. The code integrating the 2D reduced model was elaborated on the same architecture, with one dimension suppressed.

Simulations were realized on the massively parallel Compaq alpha-cluster (TERA) of the CEA. Up to 128 processors were employed for runs consuming several thousands of

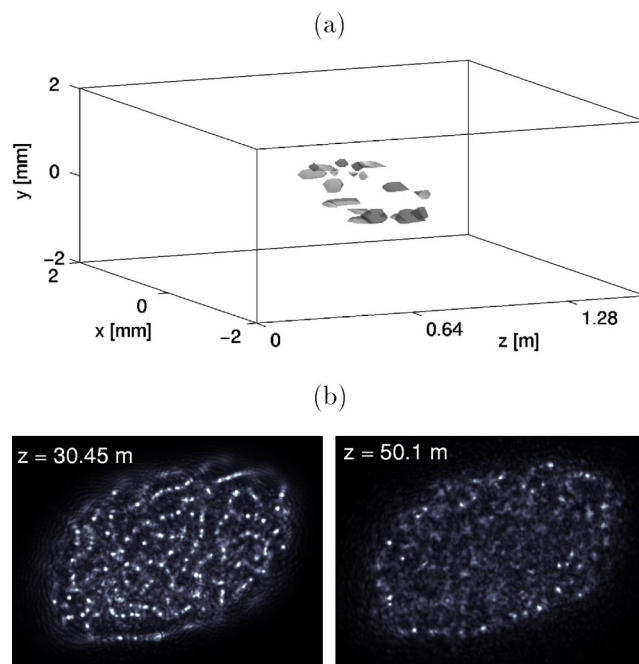


FIG. 13. Underresolved (3D+1) numerical results with spatial stepsize $\Delta x = \Delta y \approx 100 \mu\text{m}$ for the multiple filamentation patterns shown in Figs. 5(c) and 8.

CPU hours. In spite of these substantial capacities, (3D+1)-dimensional simulations of broad (cm-waisted) pulses over several tens of meters could not be properly achieved in reasonable time. As mentioned in Sec. III A, one of the sharpest constraints met in 3D numerical computing is to solve accurately individual plasma channels, whose typical size reaches a few tens of microns only. In this regard, we find it instructive to show plots of underresolved filamentary patterns corresponding to Figs. 5(c) and 8, respectively (see Fig. 13). In this latter case, the input beam amplitude has been multiplied by a perturbed temporal Gaussian profile. Figure 13 illustrates the results of (3D+1)-dimensional simulations performed with spatial steps limited to $\sim 100 \mu\text{m}$ along the x and y directions. Underresolution leads to an artificial increase of the number of small-scale cells, caused by the coarse plasma response that cannot hold a robust channel. Energy is dissipated outwards, which contributes to increase falsely the number of light cells. The filaments finally spread out too early, compared with the experimental data and with the results yielded by the 2D model [Eq. (3)], integrated with much higher spatial resolution.

- [1] A. Braun, G. Korn, X. Liu, D. Du, J. Squier, and G. Mourou, *Opt. Lett.* **20**, 73 (1995); E. T. J. Nibbering, P. F. Curley, G. Grillon, B. S. Prade, M. A. Franco, F. Salin, and A. Mysyrowicz, *ibid.* **21**, 62 (1996).
 [2] A. Brodeur, C. Y. Chien, F. A. Ilkov, S. L. Chin, O. G. Kosareva, and V. P. Kandidov, *Opt. Lett.* **22**, 304 (1997).
 [3] B. LaFontaine, F. Vidal, Z. Jiang, C. Y. Chien, D. Comtois, A.

Desparois, T. W. Johnston, J.-C. Kieffer, H. Pépin, and H. P. Mercure, *Phys. Plasmas* **6**, 1615 (1999).

- [4] S. L. Chin, A. Talebpour, J. Yang, S. Petit, V. P. Kandidov, O. G. Kosareva, and M. P. Tamarov, *Appl. Phys. B: Lasers Opt.* **74**, 67 (2002).
 [5] S. Tzortzakis, L. Bergé, A. Couairon, M. Franco, B. Prade, and A. Mysyrowicz, *Phys. Rev. Lett.* **86**, 5470 (2001).

- [6] D. Mondelain, Ph.D. thesis No. 212-2001, Université Cl. Bernard, Lyon 1, France 2001, p. 121.
- [7] L. Bergé, S. Skupin, F. Lederer, G. Méjean, J. Yu, J. Kasparian, E. Salmon, J. P. Wolf, M. Rodriguez, L. Wöste, R. Bourayou, and R. Sauerbrey, *Phys. Rev. Lett.* **92**, 225002 (2004).
- [8] L. Wöste, C. Wedekind, H. Wille, P. Rairoux, B. Stein, S. Nikolov, Ch. Werner, St. Niedermeier, F. Ronneberger, H. Schillinger, and R. Sauerbrey, *Laser Optoelektron.* **29**, 51 (1997).
- [9] V. I. Bespalov and V. I. Talanov, *JETP Lett.* **3**, 307 (1966).
- [10] J. H. Marburger, *Prog. Quantum Electron.* **4**, 35 (1975).
- [11] L. Bergé, Cl. Gouédard, J. Schjødt-Eriksen, and H. Ward, *Physica D* **176**, 181 (2003).
- [12] S. Skupin, U. Peschel, C. Etrich, L. Leine, D. Michaelis, and F. Lederer, *Opt. Lett.* **27**, 1812 (2002).
- [13] M. Mlejnek, M. Kolesik, J. V. Moloney, and E. M. Wright, *Phys. Rev. Lett.* **83**, 2938 (1999).
- [14] H. Wille, M. Rodriguez, J. Kasparian, D. Mondelain, J. Yu, A. Mysyrowicz, R. Sauerbrey, J.-P. Wolf, and L. Wöste, *Eur. Phys. J.: Appl. Phys.* **20**, 183 (2002); J. Kasparian, M. Rodriguez, G. Méjean, J. Yu, E. Salmon, H. Wille, R. Bourayou, S. Frey, Y. B. André, A. Mysyrowicz, R. Sauerbrey, J.-P. Wolf, and L. Wöste, *Science* **301**, 61 (2003).
- [15] M. Mlejnek, E. M. Wright, and J. V. Moloney, *Opt. Lett.* **23**, 382 (1998).
- [16] S. L. Chin, A. Brodeur, S. Petit, O. G. Kosareva, and V. P. Kandidov, *J. Nonlinear Opt. Phys. Mater.* **8**, 121 (1999).
- [17] A. Couairon, S. Tzortzakis, L. Bergé, M. Franco, B. Prade, and A. Mysyrowicz, *J. Opt. Soc. Am. B* **19**, 1117 (2002).
- [18] H. Ward and L. Bergé, *Phys. Rev. Lett.* **90**, 053901 (2003).
- [19] R. Y. Chiao, E. Garmire, and C. H. Townes, *Phys. Rev. Lett.* **13**, 479 (1964).
- [20] N. G. Vakhitov and A. A. Kolokolov, *Izv. Vyssh. Uchebn. Zaved., Radiofiz.* **16**, 1020 (1973) [*Radiophys. Quantum Electron.* **16**, 783 (1975)]; A. A. Kolokolov, *ibid.* **17**, 1332 (1974) [*Radiophys. Quantum Electron.* **17**, 1016 (1976)].
- [21] E. A. Kuznetsov, A. M. Rubenchik, and V. E. Zakharov, *Phys. Rep.* **142**, 103 (1986).
- [22] M. I. Weinstein, *Commun. Pure Appl. Math.* **39**, 51 (1986).
- [23] See, for review, L. Bergé, *Phys. Rep.* **303**, 259 (1998).
- [24] F. Courvoisier, V. Boutou, J. Kasparian, E. Salmon, G. Méjean, J. Yu, and J.-P. Wolf, *Appl. Phys. Lett.* **83**, 213 (2003).
- [25] S. Skupin, L. Bergé, U. Peschel, and F. Lederer, *Phys. Rev. Lett.* **93**, 023901 (2004).
- [26] G. P. Agrawal, *Nonlinear Fiber Optics*, 3rd Ed. (Academic Press, New York, 2001), p. 274; L. Bergé, J. Juul Rasmussen, E. A. Kuznetsov, E. G. Shapiro, and S. K. Turitsyn, *J. Opt. Soc. Am. B* **13**, 1879 (1996).
- [27] M. Rodriguez, R. Bourayou, G. Méjean, J. Kasparian, J. Yu, E. Salmon, A. Scholz, B. Stecklum, J. Eisloffel, U. Laux, A. P. Hatzes, R. Sauerbrey, L. Wöste, and J.-P. Wolf, *Phys. Rev. E* **69**, 036607 (2004).